Phase Transition of Magnetite Ore Fines During Oxidation Probed by *In Situ* High-Temperature X-Ray Diffraction

HENG ZHENG, ODAY DAGHAGHELEH, YAN MA, BERND TAFERNER, JOHANNES SCHENK, and YURY KAPELYUSHIN

The reduction of magnetite-based iron ore fines in a hydrogen-induced fluidized bed becomes an attractive fossil-free ironmaking route. Our previous study showed that a prior oxidation treatment of magnetite was helpful to improve its fluidization and reduction behavior. However, the underlying oxidation mechanisms of magnetite ore fines remained unclear and required further investigations. In this study, two magnetite ore brands were analyzed *via in situ* high-temperature X-ray diffraction (HT-XRD) during oxidation, to investigate the thermal transformation of Fe_3O_4 to $\alpha\text{-}Fe_2O_3$ at crystal scale. The lattice constants and crystallite sizes of both phases and oxidation degree were evaluated at different temperatures based on the HT-XRD patterns. The lattice constants of Fe_3O_4 and $\alpha\text{-}Fe_2O_3$ increased with an increase in temperature due to the thermal expansion and can be successfully fitted with temperature by second-order polynomials. With Fe_3O_4 being oxidized into Fe_2O_3, the Fe_2O_3 crystallite grew and showed a certain growth habit. The Fe_2O_3 crystallite grew faster along the a/b axis than the c axis. The oxidation kinetics followed the parabolic law as shown by the sigmoid-shaped oxidation degree curve, suggesting that the solid diffusion of ions was the rate-limiting step.

I. INTRODUCTION

MAGNETITE ore is one of the important resources for ironmaking plants. The global magnetite ore production is approximately 583 million tons per year accounting for 28 pct of the total iron ore production.[1] In some countries, such as South Australia, the major iron ore deposit is magnetite.[2] The current commercial practice of magnetite ore fines usually requires pelletization to produce iron ore pellets with appropriate size and strength.[3] However, the pelletizing process requires additional energy and cost and generates CO_2 emissions.

HENG ZHENG, ODAY DAGHAGHELEH, and BERND TAFERNER are with the Montanuniversitaet Leoben, Franz-Josef-Straße 18, 8700 Leoben, Austria. Contact email: heng.zheng@stud.unileoben.ac.at YAN MA is with the Max-Planck-Institut für Eisenforschung, Max-Planck-Straße 1, 40237, Düsseldorf, Germany. JOHANNES SCHENK is with the Montanuniversitaet Leoben and also with the K1-MET GmbH, Stahlstraße 14, 4020 Linz Austria. Contact e-mail: johannes.schenk@unileoben.ac.at YURY KAPELYUSHIN is with the South Ural State University (National Research University), Lenina Avenue 76, Chelyabinsk, Russian Federation 454080.

One possible concept for future crude steel production is using a hydrogen-based fluidized bed to produce hydrogen direct reduced iron (HDRI), followed by an electric arc furnace (EAF) process.[4,5] Therefore, the production of HDRI using magnetite ore fines in a hydrogen-induced fluidized bed becomes of great interest. The hydrogen-based fine-ore reduction (HYFOR) process developed by Primetals Technologies is one of the successful examples. The HYFOR process allows for the operation of any type of iron ore fines with particle sizes of 100 pct < 150 μm.[6] In the case of using magnetite ore fines, prior oxidation occurs in the preheating stage. A series of laboratory-scale experiments showed that the prior oxidation of magnetite was helpful to improve its fluidization and reduction behavior.[7–9] Thus, it is of great importance to understand the oxidation mechanisms of magnetite ore fines for optimizing the process route.

The exothermic effect, structural evolution, and kinetic analysis regarding the oxidation of magnetite were summarized in our previous work.[10,11] In general, the oxidation of magnetite experienced two stages, where the magnetite was oxidized into an intermediate phase and further oxidized to $\alpha\text{-}Fe_2O_3$. During the oxidation, whisker or rough pleated structures of hematite were formed on the surface of magnetite particles. The rate-limiting step for oxidation of

magnetite in particle scale was generally solid-state diffusion which can be well described by parabolic law. The diffusion of oxygen into/within the magnetite particles was not the rate-limiting step. There are many kinetic studies on the oxidation of magnetite at the particle scale using thermogravimetric analysis (TGA).[12–16] In addition, some post-mortem X-ray diffraction (XRD) measurements were conducted to study crystal transformation after the oxidation of magnetite. It was found that magnetite from different mines showed different lattice constants due to various types of gangue elements.[17] .The lattice constant of oxidized magnetite also differed after oxidation at different temperatures.[18] The strain/stress occurring in the lattice should promote the nucleation of α-Fe_2O_3 and the crystallite size of magnetite governed the formation of γ-Fe_2O_3 and the oxidation kinetics.[19] The crystallite size of the oxidized magnetite calculated based on the Scherrer equation was comparable to that measured by transmission electron microscopy (TEM), which proved the accuracy of the XRD method for obtaining the crystallite size.[20] However, little information is available in the literature on the phase transition at the crystal scale during oxidizing magnetite, which limits the understanding of the oxidation mechanisms of magnetite. The objective of the present study is to investigate the thermal transformation of magnetite ore fines at the crystal scale *via in situ* high-temperature XRD (HT-XRD) during oxidation. The findings provide deeper insights into the phase transformation from magnetite to hematite under an oxidation condition.

II. EXPERIMENTAL PROCEDURES

A. *Materials*

Two commercial magnetite ore brands were investigated in this study and their chemical compositions are listed in Table I. The particle size distributions and apparent densities of the ores were characterized by CILAS 1064 particle size analyzer and Ultrapycnometer 1000 density analyzer, respectively. The results are listed in Table II. The raw ores were dried at 110 °C for 6 h before all the following tests.

B. *In Situ High-Temperature X-Ray Diffraction (HT-XRD)*

The HT-XRD analyses were performed on a Rigaku Ultima IV XRD diffractometer with a Cu target. The Kα radiation was filtered as the X-ray source. The measurement step size was 0.02 deg and the sampling time was 0.15 s/step. In each measurement, 300 mg of material was placed on a platinum heating strip and heated in the HTK-16 high-temperature chamber (Anton Paar) to 1000 °C at a heating rate of 100 °C/ min. The material was placed in a very thin layer to avoid thermal gradients along the height. It is difficult to determine the thickness of the layer. The layer was composed of a stack of approximately 3 magnetite particles and supposed to be thinner than 150 μm. The *in situ* HT-XRD measurements were conducted at temperatures of 400 °C, 600 °C, 800 °C, and 1000 °C, as shown in Figure 1. The air could be exchanged between the facility chamber and the outside. Due to the small amount of magnetite, the change of oxygen partial pressure was negligible. The oxygen partial pressure was assumed to be the same as the ambient atmosphere. Before and after the oxidation experiments, the XRD measurements were conducted at room temperature with a scanning angle between 25 and 65 deg. It should be noted that the temperature ramping was halted and the material was kept at a fixed temperature during the *in situ* HT-XRD measurements. The oxidation reaction continued during the HT-XRD scans. To minimize the duration of the HT-XRD measurements and increase the time resolution, the scanning angle was set in a narrow range between 32 and 41 deg, where three hematite peaks and two magnetite peaks could be observed. In this case, each HT-XRD measurement took around 67.5 s.

C. *HT-XRD Data Treatment*

The Rietveld refinement method was widely used for phase quantification in ironmaking area.[21–24] At current study, the Jade 6.0 software provided by Materials data Inc. was employed to identify and fit the diffraction peaks in this study. The overlapped peaks of magnetite and hematite at around 35 deg were successfully

Table I. Chemical Analysis of the Raw Magnetite Samples, (Wt Pct)[11]

	Fe$_{tot}$	FeO	SiO$_2$	Al$_2$O$_3$	MgO	CaO	TiO$_2$	P	S
Ore A	68.78	27.71	5.60	0.18	0.17	0.17	—	0.017	0.05
Ore B	65.65	27.66	3.33	1.16	1.62	1.62	0.22	0.017	0.10

Table II. Particle Size Distributions and Density of the Raw Magnetite Samples[11]

	D10 (μm)	D50 (μm)	D90 (μm)	Skeletal Density (g/cm^3)
Ore A	4.81	28.35	62.66	4.94
Ore B	6.10	32.25	70.16	5.09

separated by refinement in Jade 6.0 software, and the location and profile of individual peaks were obtained, as shown in Figure 2. Besides, the quantitative information of crystal information, such as lattice constants,[25] crystallite size,[26] and phase fraction,[27] can be obtained.

1. Determination of Lattice Constants

Based on our previous TGA tests, the oxidation started at around 200 °C then reached the first peak at around 330 °C and the second peak started at around 400 °C.[11] The oxidation product was supposed to be γ-Fe_2O_3 between 200 °C and 400 °C. Above 400 °C, γ-Fe_2O_3 transformed into α-Fe_2O_3. In the present study, the oxidation temperature was higher than 400 °C, and thus only α-Fe_2O_3 was expected to be the oxidation product (hereafter, α-Fe_2O_3 is referred to as Fe_2O_3). Therefore, two crystal structures were considered: Fe_3O_4 (cubic close-packed crystal) and Fe_2O_3 (hexagonal close-packed crystal). The relationship between interplanar spacings (d), lattice constants (a), and crystal planes {hkl} are expressed in Eqs. [1] and [2].[28] When a specific plane and corresponding interplanar spacing are known, the lattice constants can be calculated. The interplanar spacing can be obtained by Bragg's law as shown in Eq. [3].

$$\text{Cubic close-packed crystal} : \frac{1}{d^2} = \frac{h^2 + k^2 + l^2}{a^2} \quad [1]$$

Hexagonal close-packed crystal :

$$\frac{1}{d^2} = \frac{4}{3}\frac{\left(h^2 + k^2 + hk\right)}{a^2} + \frac{l^2}{c^2} \quad [2]$$

$$Bragg's\ \text{law} : d = \frac{n\lambda}{2\mathrm{Sin}\theta}, \quad [3]$$

where d is the interplanar spacing; a and c are the lattice constants, {hkl} is the crystal plane; n is the diffraction order, and here the value is 1.

2. Determination of Crystallite Size

Crystallite size (D) can be calculated using the Scherrer equation, as given in Eq. [4]. It should be noted that the crystallite size refers to the average thickness perpendicular to the (hkl) planes. The (110) and (104) planes of Fe_2O_3 crystal were chosen for quantifying the crystallite size. Because these two peaks exhibit relatively high intensities and have similar instrumental broadening conditions (similar peak position).[29] As shown in Figure 3, the (110) plane is parallel to the c axis and (104) plane is at a small angle to the a/b axis.[29] Therefore, the crystallite size along the c axis and a/b axis can be calculated according to Eqs. [5], [6].

$$D = \frac{K\lambda}{\beta cos\theta} \quad [4]$$

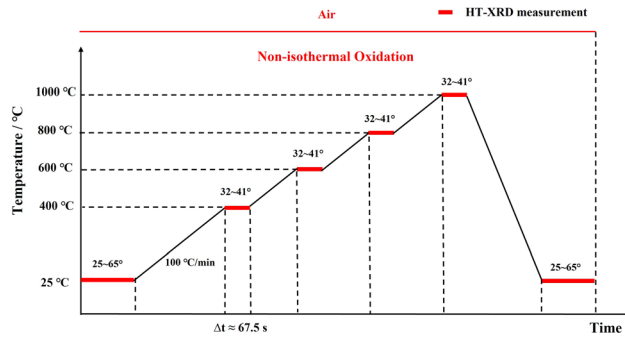$$D_{a/b} = D_{110} \times \cos\alpha_{110} \quad [5]$$

Fig. 1—Temperature profile for HT-XRD measurements.
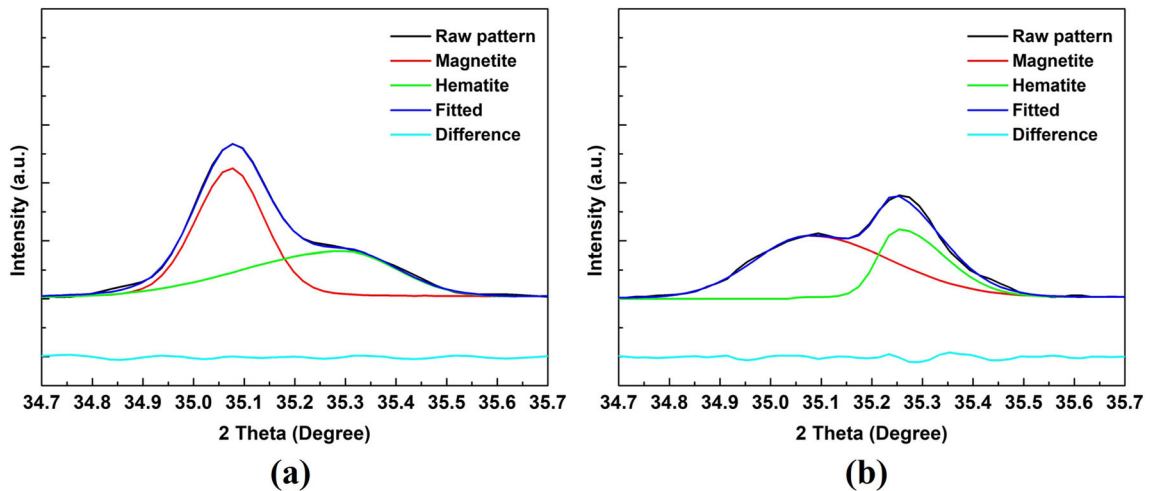

Fig. 2—Rietveld refinement peak profile of Ore A at different temperatures: (a) 600 °C and (b) 800 °C.
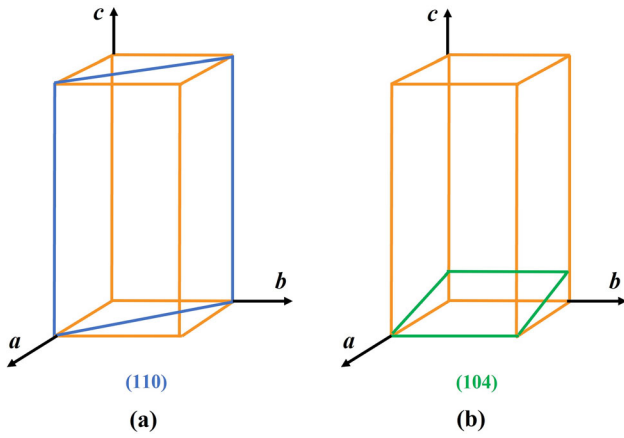
Fig. 3—Schematic of Fe_2O_3 crystal: (a) (110) plane and (b) (104) plane.

$$D_c = D_{104} \times \cos\alpha_{104}, \quad [6]$$

where D is crystallite size, nm; K is 0.94 (Scherrer constant); λ is 0.15406 nm (the wavelength of $K\alpha$ Cu X-ray source); β is full width at half maximum (FWHM), radians; θ is peak position, radians; $D_{a/b}$ and D_c represent the crystallite size calculated based on (110) and (104) peaks; α_{110} is the angle between [110] direction and $x–y$ plane; α_{104} is the angle between the [104] direction and the $y–z$ plane. Here, $\cos\alpha_{110} = 1$ and $\cos\alpha_{104} = 0.6192$.[29]

3. Determination of Oxidation Degree

The matrix-flushing method[30,31] was used to obtain the content of Fe_3O_4 and Fe_2O_3. The relative mass content of each phase is proportional to the ratio between its peak intensity and relative intensity ratio (RIR). The RIR value of each phase can be found in the PDF card database. The RIRs of the Fe_3O_4 and Fe_2O_3 phases are 4.9 and 3.2, respectively. The impurities were not considered in the calculation. The content of Fe_2O_3 and Fe_3O_4 can be calculated based on Eqs. [7], [8].[11]

$$\frac{x_H}{x_M} = \frac{I_H}{k_H} / \frac{I_M}{k_M} \quad [7]$$

$$x_H + x_M = 1, \quad [8]$$

where x_H and x_M are the relative mass content of Fe_2O_3 and Fe_3O_4. I_H, I_M, k_H, and k_M are the intensities and RIR values of Fe_2O_3 and Fe_3O_4, respectively.

Kapelyushin et al.[32] calculated the reduction degree of Fe_3O_4 in the CO-CO_2 atmosphere based on HT-XRD analysis. The oxidation degree of Fe_3O_4 can be obtained by a similar method. The initial mass content of Fe_3O_4 was calculated via the mass balance of iron. Hence, the theoretical weight gain can be obtained as given in Eqs. [9], [10]. The actual weight gain was calculated based on the Fe_2O_3 mass content via Eq. [11]. Thereafter, the oxidation degree (w) can be obtained by Eq. [12].[33,34]

$$m_M = x_M + \frac{x_H}{W_H} \times \frac{2}{3} \times W_M \quad [9]$$

$$\Delta m_{\text{theory}} = \frac{m_M}{W_M} \times \frac{W_O}{4} \quad [10]$$

$$\Delta m = \frac{x_H}{W_H} \times \frac{2}{3} \times \frac{W_O}{4} \quad [11]$$

$$w = \frac{\Delta m}{\Delta m_{theory}} \times 100 \text{ pct}, \quad [12]$$

where W_H, W_M, and W_O are mole masses of Fe_2O_3, Fe_3O_4, and O_2, respectively. m_M, Δm_{theory}, Δm, and w are the initial mass content of Fe_3O_4, theoretical weight gain, actual weight gain, and oxidation degree.

III. RESULTS AND DISCUSSION

A. Oxidation of Magnetite

Figure 4 shows the oxidation behavior of two ores at different temperatures probed by HT-XRD. Two ores revealed similar oxidation behavior, as suggested by the diffraction patterns. All the peaks shifted to a lower diffraction angle with an increase in temperature due to thermal expansion.[35–37] The (104) peak of Fe_2O_3 firstly appeared at 400 °C, as shown in Figures 4(a) and (c). With an increase in temperature, the intensity of the (104) peak increased, indicating a higher fraction of Fe_2O_3. The (311) peak of Fe_3O_4 vanished at 1000 °C, representing deep oxidation of Fe_3O_4. The width of (104) peak became narrower with increasing temperature, which suggested the growth of Fe_2O_3 crystallite.

B. Oxidation Degree

The oxidation degrees of both ores at different temperatures are shown in Figure 5. Ore A was easier to be oxidized than Ore B, as indicated by its faster kinetics. The oxidation degree was lower than 10 pct at 400 °C in both cases. When the temperature increased to 600 °C, the oxidation degree increased significantly. Above 800 °C, the oxidation rate slowed down. The sigmoid-shaped oxidation degree curve indicated that the kinetics followed the parabolic law, where the solid diffusion of ions was the rate-limiting step. The oxidation mechanism was explained in our previous study.[11] Each magnetite crystal unit contains eight Fe_3O_4 molecules, i.e., 32 oxygen anions and 24 iron cations (16 Fe^{3+} and 8 Fe^{2+}). The oxygen anions present a cubic close-packed structure, where 96 interstices exist. Only 8 out of 64 tetrahedral interstices are occupied by Fe^{3+} cations. 16 out of 32 octahedral interstices are occupied by 8 Fe^{3+} cations and 8 Fe^{2+} cations.[11] Due to so many interstices, the iron cations can move easily within the crystal lattice. The
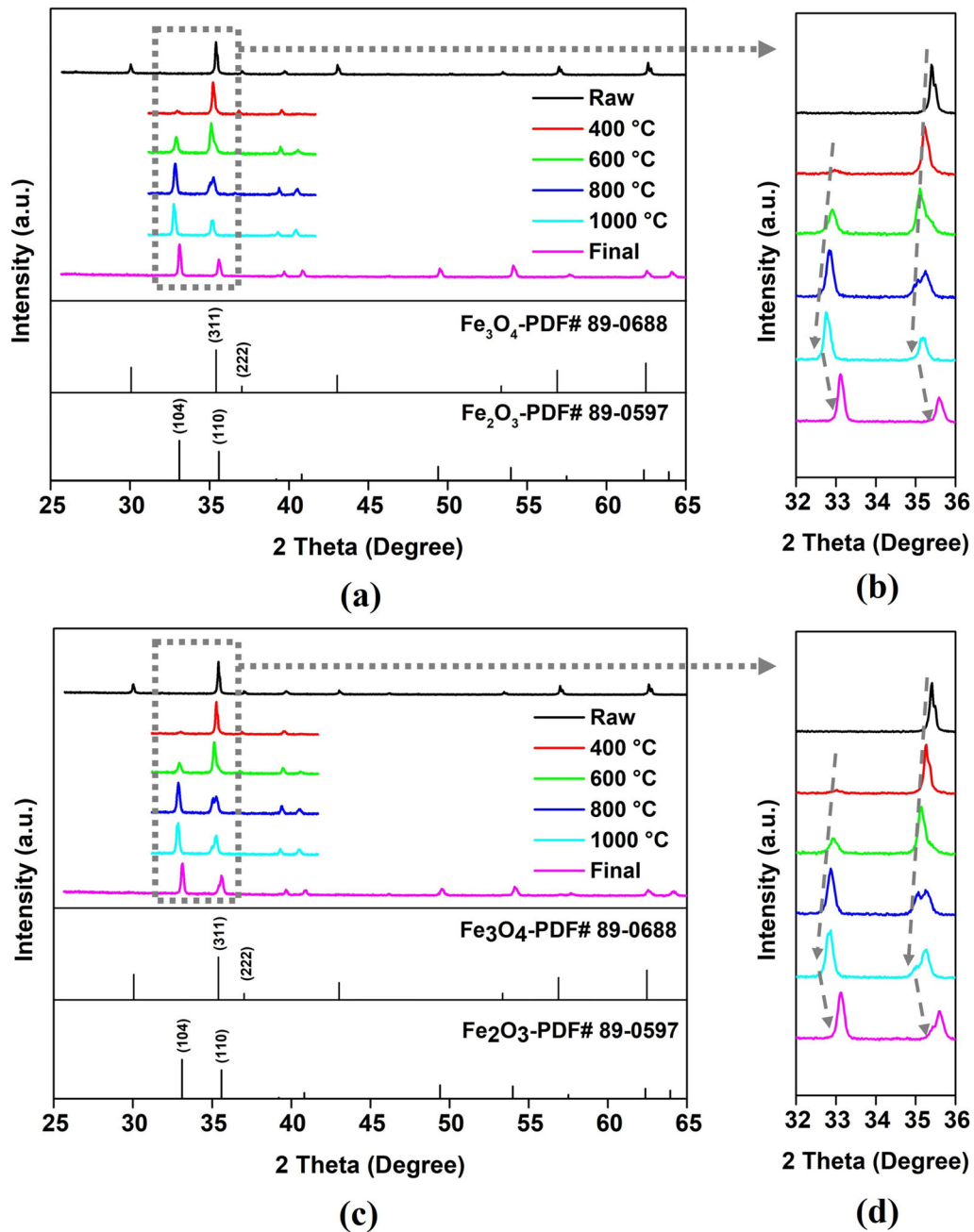
Fig. 4—*in situ* HT-XRD patterns at different temperatures: (*a*), (*b*) Ore A; (*c*), (*d*) Ore B.

O^{2-} anion can hardly move due to its bigger size. From the crystal scale, when an oxygen atom is trapped by Fe_3O_4 for phase transformation, two electrons are taken from the crystal by the oxygen atom. In the meanwhile, two positively charged holes 2 h + are generated in the place of the previous electrons for a neutral local charge in the crystal. Then Fe^{2+} cation may capture the charged hole h^+ and becomes Fe^{3+} cation. In later oxidation stage, due to the high amount of Fe^{3+} cations, the charged hole h^+ has less opportunity to meet Fe^{2+} cations. In the contrast, the charged hole h^+ decreases the mobility of the iron cations and expand the crystal unit.

C. Evolution of Lattice Constants

Table III summarizes the lattice constants of Fe_3O_4 in the ores at different temperatures. The results are comparable to those in the literature. The change in lattice constant with increasing temperature is supposed to be caused by thermal expansion and lattice modification during oxidation.[18] As shown in Table III, the lattice constant at a specific temperature measured in this study was slightly larger than that in the literature. Such a difference might be due to a much higher oxygen partial pressure in the present study, as the magnetite was oxidized under an air atmosphere. This condition could result in a larger lattice constant of magnetite due
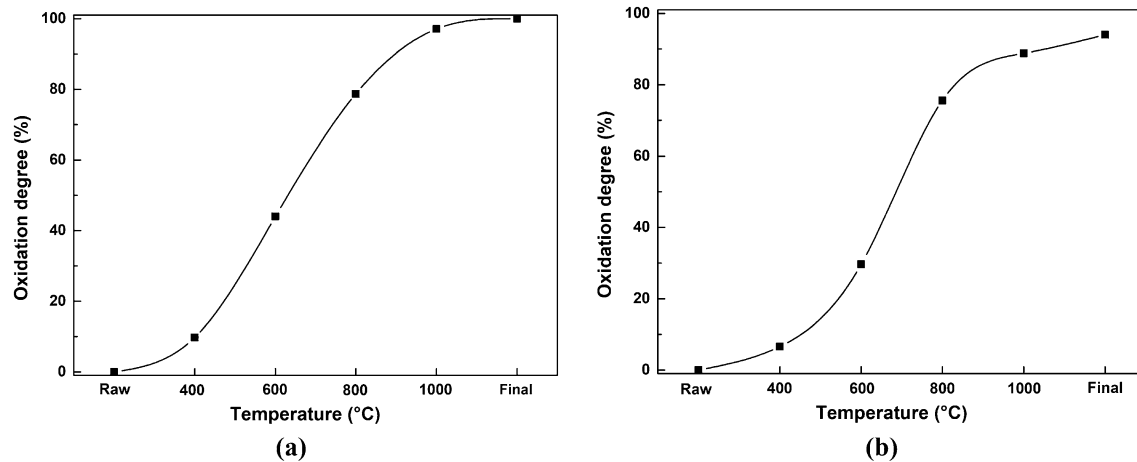
Fig. 5—The oxidation degrees of Ore A and B at different temperatures: (*a*) Ore A; (*b*) Ore B.

to partial oxidation[38] (*i.e.*, a higher oxygen occupancy in the lattice). The temperature dependence of the lattice constant can be represented by polynomials up to the fifth order.[39] Here, the relation between lattice constant and temperature was successfully fitted with the second-order polynomials (Figure 6), within a temperature range of 25 °C to 800 °C. The temperature-dependent lattice constant of Fe_3O_4 can be described as follows: $a = 2.53 \times 10^{-8} \times T^2 + 8.64 \times 10^{-5} \times T + 8.4132$. At the higher temperature (e.g., 1000 °C), the (222) peak of Fe_3O_4 disappeared, which reduced the accuracy in the assessment of the lattice constant. Thus, the lattice constant at 1000 °C was not considered.

Table IV lists the lattice constants of Fe_2O_3 at different temperatures. Based on Eq. [2], at least two peaks of Fe_2O_3 are required to obtain the lattice constant *a* and *c* for a trigonal crystal structure. Therefore, only one set of *a* and *c* can be calculated at each temperature in the current study. The lattice parameters of Fe_2O_3 measured in this study were slightly larger than those in the literature, where *a* was 5.01 to 5.04 Å and *c* was 13.68 to 13.73 Å in the temperature range of 300 °C to 800 °C.[41] Stefano *et al.*[37] studied the phase transformation from goethite (α-FeOOH) to hematite (α-Fe_2O_3) in the temperature range of 200 °C to 1000 °C by synchrotron powder diffraction. Hematite was formed by the release of the OH^- groups of goethite phase. The hexagonally close-packed arrays of oxygen anions present in the parent goethite still remained in the newly formed hematite. Tatsuo *et al.*[42] studied the thermal expansion of hematite at high temperatures, where no chemical reaction occurred. In current study, the hematite was formed by the oxidation of magnetite. The oxygen anions are transferred from cubic close-packed arrays to the hexagonally close-packed arrays. The aforementioned three hematite phases were generated through distinct pathways. Figure 7 shows the relative increase in *a* and *c* of the three hematite phases. The correlation between lattice constants and temperature can be also fitted with second-order polynomials (Figure 8). The temperature-dependent lattice constant of Fe_2O_3 can be

described as follows: $a = -2.81 \times 10^{-8} \times T^2 + 8.76 \times 10^{-5} \times T + 5.0368$; $c = 3.01 \times 10^{-8} \times T^2 + 1.09 \times 10^{-4} \times T + 13.7621$.

The SiO_2 was the dominant impurity in both ores. At current study, the maximum temperature was 1000 °C, the SiO_2 was considered as inert phase. The size of Mg^{2+} (72 pm) is similar to Fe^{2+} (74 pm). Therefore, the influence of SiO_2 and MgO on the lattice constant was ignored. The ore B contains more gangue minerals than the ore A. The impurities such as Al_2O_3 and CaO should have influence on the crystal cell of Fe_3O_4 and Fe_2O_3. Due to the smaller size of Al^{3+} (54 pm) than Fe^{3+} (65 pm), the substitution of Fe^{3+} by Al^{3+} in Fe_3O_4 or Fe_2O_3 crystal cell would result in a contraction of the cell volume. The Ca^{2+} cations either displace Fe^{2+} or occupy vacancies in Fe_3O_4 cell, both of which may result in an expansion of the crystal cell duo to the larger size of Ca^{2+} (100 pm). In other words, the Al^{3+} and Ca^{2+} show the opposite effect on the crystal size of Fe_3O_4 cell. Figure 9(a) illustrates the expansion of Fe_3O_4 crystal cell at different temperatures. The difference between the Ore A and Ore B was not significant. The Fe_3O_4 crystal cell expansion rate of Ore B was slightly smaller than that of Ore A, which can be explained by the substitution of Fe^{3+} by Al^{3+}. However, the expansion rate at 800 °C was an exception. The Al^{3+} cations had better mobility within the Fe_3O_4 crystal cell than that of Ca^{2+} cations. Only at high temperature, i.e., 800 °C, the effect of Ca^{2+} cations became more dominant than Al^{3+} cations and promoted the expansion of the Fe_3O_4 crystal cell. Figure 9(b) shows the expansion of Fe_2O_3 crystal cell at different temperatures. The Fe_2O_3 crystal cell expansion rate of Ore B was slightly larger than that of Ore A at 600 °C and became more obvious at 800 °C. While at 1000 °C, the expansion rate of Ore B was smaller than that of Ore A. This phenomenon could be also explained by the combined effect of Al^{3+} and Ca^{2+} cations in the Ore B. Based on the stability diagram of Fe_3O_4-$FeAl_2O_4$ and Fe_2O_3-$FeAlO_3$, Al^{3+} cations prefer to combine with Fe_3O_4 to form magnetite-based solid solution.[43] At 1000 °C, the

Table III. The Lattice Constant and Volume of the Fe₃O₄ Cell Measured by High-Temperature X-Ray Diffraction During the Oxidation of Fe₃O₄ in Air

Temp	Ore A		Ore B		**Ref. 40	**Ref. 38
	$a = b = c$ (Å)	Volume (Å³)	$a = b = c$ (Å)	Volume (Å³)	$a = b = c$ (Å)	$a = b = c$ (Å)
25 °C	8.4156 ± 0.0021	596.0207	8.4165 ± 0.0007	596.2214	8.3778	—
400 °C	8.4476 ± 0.0035	602.8437	8.4473 ± 0.0010	602.7819	8.4203	8.3888
600 °C	8.4796 ± 0.0010	609.7186	8.4797 ± 0.0005	609.7486	8.4547	8.4424
800 °C	8.4953 ± 0.0042	613.1268	8.4974 ± 0.0005	613.5637	8.4761	8.4698
*1000 °C	—	—	—	—	8.4969	8.4987

*The intensity of Fe₃O₄ peaks at 1000 °C is quite low and not suitable for the calculation of lattice constant.
**The lattice constant from Refs. 40 and 38 are the values measured at vacuum conditions.
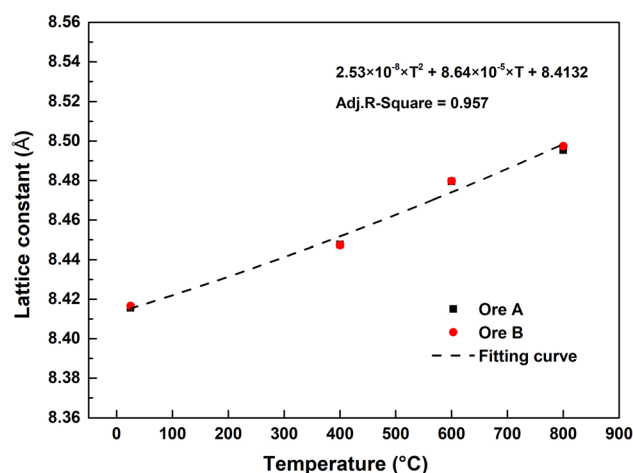
Fig. 6—The lattice constant of Fe₃O₄ as a function of temperature measured by high-temperature X-ray diffraction during oxidation of Fe₃O₄ in air.

Fig. 7—The relative increase in lattice parameters a and c of Fe₂O₃ at different temperatures[37,42]

oxidation degree of Ore B was 88.8 pct. With the decrease of magnetite phase, the Al^{3+} cations diffused from magnetite to hematite phase, resulting in the lower expansion rate of Ore B.

D. Evolution of Crystallite Size of Fe₂O₃

Figure 10 shows the Fe₂O₃ crystallite sizes of Ore A and B along the c axis and the a/b axis. With an increase in temperature, more and more Fe₃O₄ was oxidized into Fe₂O₃, and thus the Fe₂O₃ crystallite in both ores grew, as shown in Figure 10. It was also observed in both ores that Fe₂O₃ grew faster along a/b axis ($D_{a/b}$ in Figure 10) than c axis (D_c in Figure 10) in the crystal unit, especially in the beginning of oxidation. Also, the crystallite size along the a/b axis revealed a larger size than that along the c axis. Such findings suggested a growth habit of Fe₂O₃ during oxidation. It is worth noting that $D_{a/b}$ and D_c were calculated based on the (110) and (104) peaks, respectively. In our previous study,[11] it was found that the surface energy of the (110) crystal surface was larger than that of the (104) crystal surface. The growth rates of the crystal faces are proportional to their surface energies, indicating a larger crystallite size along the a/b axis, which concurs well with the current study. The growth habit of Fe₂O₃ was
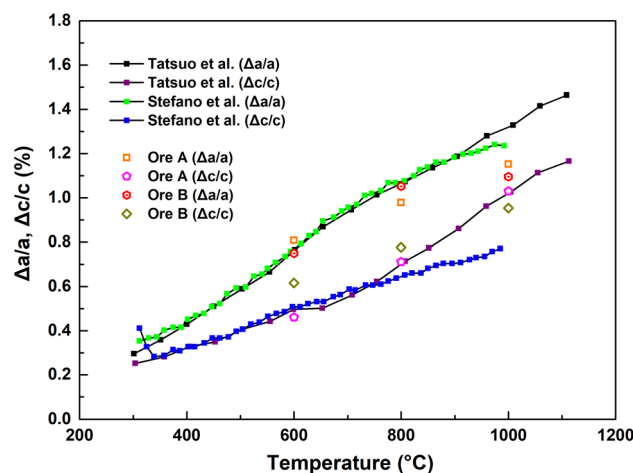
also observed in TEM micrographs of Fe₂O₃ during the decomposition of goethite, where the Fe₂O₃ phase showed acicular morphology.[44] In general, it is believed that the Fe₂O₃ phase presents acicular microcrystals due to its crystallographic-dependent properties. Besides, the crystallite sizes of Ore A were slightly larger than that of Ore B at specific temperatures. It cannot be explained with present experimental data. It may be because of the higher contents of Al₂O₃ and MgO in Ore B, which inhibit the diffusion of Fe cations.[45,46] On the other hand, the crystallite sizes, calculated based on the peak (311), of the parent Fe₃O₄ phase of the Ore A and Ore B are 1027.7 Å and 812.6 Å, respectively. The larger crystallite size of Fe₂O₃ might inherit from the larger parent Fe₃O₄ phase.

IV. CONCLUSIONS

In this study, the thermal transformation of two magnetite ore fines was investigated using *in situ* high-temperature X-ray diffraction (HT-XRD) during oxidation. The following conclusions can be obtained:

(1) The crystal information, such as lattice constant and crystallite size, can be successfully characterized by HT-XRD. The peaks in HT-XRD patterns shifted to a lower diffraction angle with an increase in

Table IV. The Lattice Constant and Volume of the Fe₂O₃ Cell

Temp	Ore A			Ore B		
	$a = b$ (Å)	c (Å)	Volume (Å³)	$a = b$ (Å)	c (Å)	Volume (Å³)
25 °C	5.0391	13.7648	302.6958	5.0391	13.7648	302.6958
*400 °C	—	—	—	—	—	—
600 °C	5.0798	13.8282	309.0220	5.0769	13.8496	309.1470
800 °C	5.0884	13.8628	310.8451	5.0921	13.8717	311.4972
1000 °C	5.0972	13.9066	312.9067	5.0943	13.896	312.3125

*The intensity of Fe₂O₃ peaks at 400 °C is quite low and not suitable for the calculation of lattice constant.
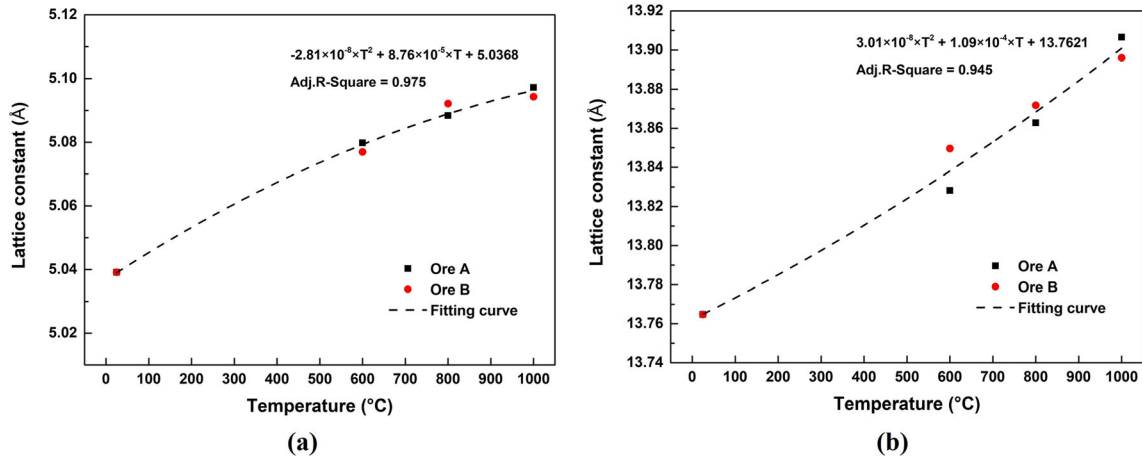
Fig. 8—The lattice constants of Fe₂O₃ as a function of temperature: (*a*) lattice constant a; (*b*) lattice constant c.
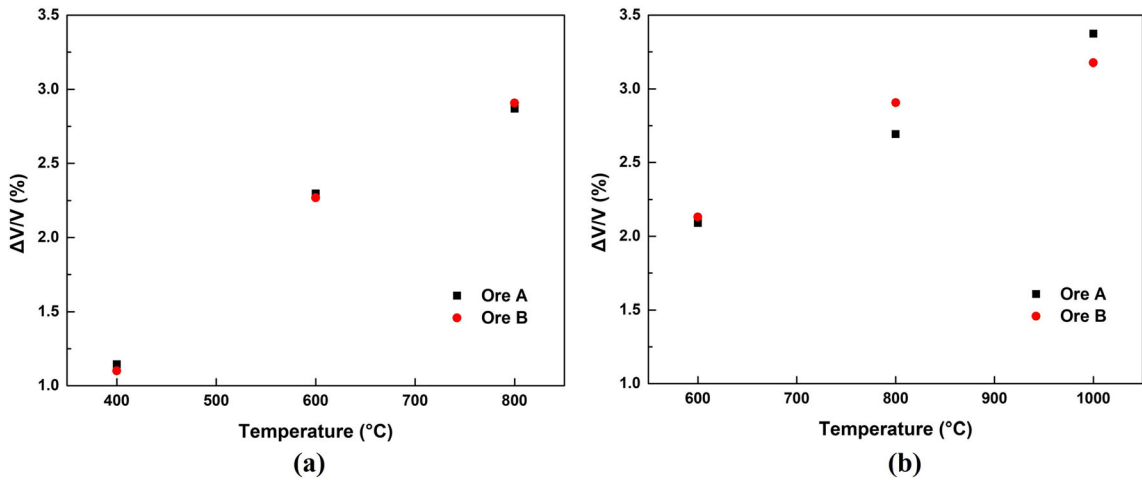
Fig. 9—The expansion of crystal cell volume as a function of temperature: (*a*) Fe₃O₄; (*b*) Fe₂O₃.

temperature due to thermal expansion. The intensity of the (104) peak of Fe₂O₃ increased with the increasing temperature, indicating an increase in the fraction of Fe₂O₃. The width of the (104) peak became narrower with the increasing temperature,

suggesting a growing crystallite size of Fe₂O₃ during oxidation.

(2) The lattice constants of Fe₃O₄ and Fe₂O₃ both increased with the temperature and followed second-order polynomials. The correlation of lattice
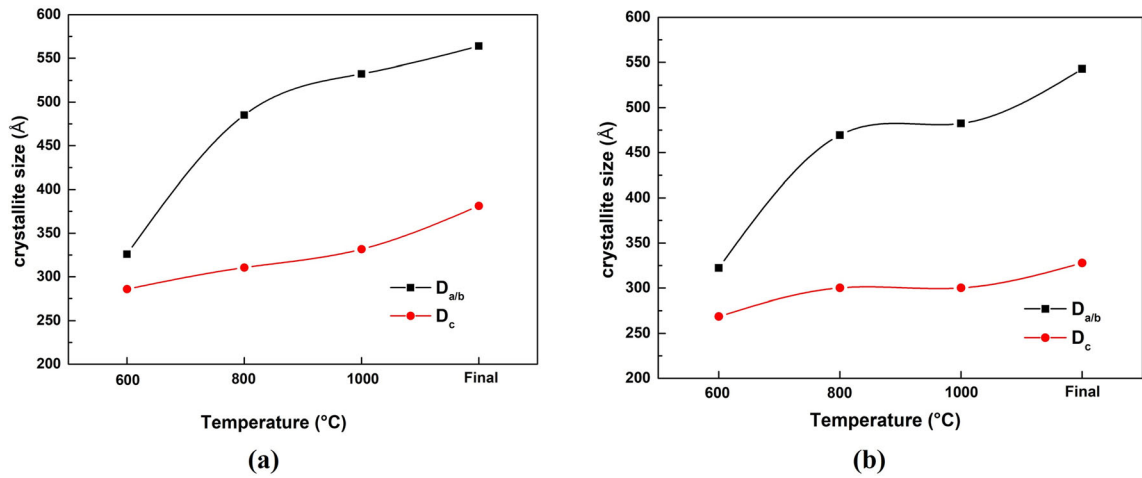
Fig. 10—The crystallite sizes of Ore A and B along the *a/b* axis and the *c* axis of a crystal cell at different temperatures: (*a*) Ore A; (*b*) Ore B.

constant and temperature can be expressed as follows:

$$Fe_3O_4 : a = 2.53 \times 10^{-8} \times T^2 + 8.64 \times 10^{-5} \times T + 8.4132;$$

$$Fe_2O_3 : a = -2.81 \times 10^{-8} \times T^2 + 8.76 \times 10^{-5} \times T + 5.0368; c = 3.01 \times 10^{-8} \times T^2 + 1.09 \times 10^{-4} \times T + 13.7621.$$

(3) During oxidation, Fe_3O_4 transformed into Fe_2O_3. The growth of Fe_2O_3 revealed a certain growth habit. The growth rates of Fe_2O_3 crystallite along the *a/b* axis was faster than that in the *c* axis, thus showing acicular microcrystals. Such a morphology may affect the subsequent reduction, which requires further investigations.

CONFLICT OF INTEREST

On behalf of all authors, the corresponding author states that there is no conflict of interest.

REFERENCES

1. Department of the Premier and Cabinet: South Australia's Magnetite Strategy: Making our state's magnetite the world's choice for steelmaking, p. 7, https://sarigbasis.pir.sa.gov.au/WebtopEw/ws/samref/sarig1/image/DDD/BROCH028.pdf. Accessed 6 Aug 2022.
2. Government of South Australia: Magnetite: South Australia's potential (2018), https://www.energymining.sa.gov.au/industry/geological-survey/mesa-journal/previous-feature-articles/magnetite_south_australias_potential. Accessed 6 Aug 2022.
3. D. Zhu, J. Pan, L. Lu, and R. J. Holmes: *Iron Ore*, 2015, pp. 435–73.
4. SALCOS®: SALCOS Official webpage (31.01.2021), https://salcos.salzgitter-ag.com/en/. Accessed 31 January 2021.
5. V. Vogl, M. Åhman, and L.J. Nilsson: *J. Clean. Prod.*, 2018, vol. 203, pp. 736–45.
6. S. Daniel, W. Johann, H. Bernhard, R. Norbert, W. Thomas, S. Wolfgang, and F. Alexander: *Mitsubishi Heavy Ind. Tech. Rev.*, 2022, vol. 59, pp. 1–5.
7. Daniel Spreitzer: Ph.D. Thesis, Montanuniversitaet Leoben, Leoben, Austria, 2020. https://pure.unileoben.ac.at/portal/files/6390410/AC16176350.pdf.
8. H. Zheng, D. Spreitzer, T. Wolfinger, J. Schenk, and R. Xu: *Metall. Mater. Trans. B*, 2021, vol. 52B, pp. 1955–71.
9. H. Zheng, O. Daghagheleh, T. Wolfinger, B. Taferner, J. Schenk, and R. Xu: *Int. J. Miner. Metall. Mater.*, 2022, vol. 28, pp. 1873–81.
10. H. Zheng, J. Schenk, D. Spreitzer, T. Wolfinger, and O. Daghagheleh: *Steel Res. Int.*, 2021, pp. 2000687.
11. H. Zheng, J. Schenk, R. Xu, O. Daghagheleh, D. Spreitzer, T. Wolfinger, D. Yang, and Y. Kapelyushin: *Metall. Mater. Trans. B*, 2022, vol. 53B, pp. 1644–60.
12. H.J. Cho, M. Tang, and P.C. Pistorius: *Metall. Mater. Trans. B*, 2014, vol. 45B, pp. 1213–20.
13. H.J. Cho and P.C. Pistorius: *AISTech Conf.*, Association for Iron & Steel Technology (AIST), Atlanta, GA, 2012, pp. 503–11.
14. T. K. Sandeep Kumar, N. N. Viswanathan, H. Ahmed, A. Dahlin, C. Andersson, and B. Bjorkman: *Metall. Mater. Trans. B.*, 2019, vol. 50, pp. 150–61.
15. A. Sardari, E.K. Alamdari, M. Noaparast, and S.Z. Shafaei: *Int. J. Miner. Metall. Mater.*, 2017, vol. 24, pp. 486–92.
16. E.R. Monazam, R.W. Breault, and R. Siriwardane: *Ind. Eng. Chem. Res.*, 2014, vol. 53, pp. 13320–28.
17. E.R. Schmidt and F.H. Vermaas: *Am. Miner.*, 1955, vol. 40, pp. 422–31.
18. K.V.G.K. Gokhale: *Econ. Geol.*, 1961, vol. 56, pp. 963–71.
19. B. Gillot, A. Rousset, and G. Dupre: *J. Solid State Chem.*, 1978, vol. 25, pp. 263–71.
20. A.-F. Lehlooh, S. Mahmood, and I. Abu-Aljarayesh: *J. Magn. Magn. Mater.*, 1994, vol. 136, pp. 143–48.
21. B.I. Whittington: *Metall. Mater. Trans. B*, 2000, vol. 31B, pp. 1175–86.
22. S. Swanepoel, A.M.G. Craig, and J.P.R. Villiers: *Metall. Mater. Trans. B.*, 2022, vol. 53B, pp. 3805–24.
23. V.D.A. Oliveira, R.D.J.T. Lana, H.C.D.S. Coelho, G.J.S. Brigolini, and C.G.D. Santos: *Metall. Mater. Trans. B*, 2020, vol. 51B, pp. 1418–31.
24. H.H. Zhu, J. Chen, J.X. Deng, R.B. Yu, and X.R. Xing: *Metall. Mater. Trans. B.*, 2012, vol. 43B, pp. 494–502.
25. Z.Y. Wang, J.L. Zhang, X.D. Xing, Z.J. Liu, Y.P. Zhang, X.L. Liu, and Y.R. Liu: *JOM*, 2016, vol. 68, pp. 656–67.
26. H. Sun, A.A. Adetoro, F. Pan, Z. Wang, and Q. Zhu: *Metall. Mater. Trans. B.*, 2017, vol. 48B, pp. 1898–1907.
27. X. Fu, Y. Wang, and F. Wei: *Metall. Mater. Trans. A.*, 2010, vol. 41A, pp. 1338–48.
28. R.J.D. Tilley: *Crystals and Crystal Structures*, Wiley, Chichester, 2006, p. 36.
29. E. Eneroth and C. Bender Koch: *Minerals Engineering*, 2003, vol. 16, pp. 1257–67.
30. F.H. Chung: *J. Appl. Crystallogr*, 1974, vol. 7, pp. 519–25.
31. F.H. Chung: *J. Appl. Cryst*, 1974, vol. 7, pp. 526–31.
32. Y. Kapelyushin, Y. Sasaki, J. Zhang, S. Jeong, and O. Ostrovski: *Metall. Mater. Trans. B.*, 2015, vol. 46B, pp. 2564–72.
33. D. Zhu, C. Yang, J. Pan, and X. Li: *Metall. Mater. Trans. B.*, 2016, vol. 47B, pp. 2919–30.
34. F. Pan, Q. Zhu, Z. Du, and H. Sun: *J. Iron Steel Res. Int.*, 2016, vol. 23, pp. 1160–67.
35. L. Kurpaska: *J. Mol. Struct.*, 2018, vol. 1163, pp. 287–93.
36. S.K. Bhargava, A. Garg, and N.D. Subasinghe: *Fuel*, 2009, vol. 88, pp. 988–93.
37. S. Gialanella, F. Girardi, G. Ischia, I. Lonardelli, M. Mattarelli, and M. Montagna: *J. Therm. Anal. Calorim.*, 2010, vol. 102, pp. 867–73.
38. D. Levy, G. Artioli, and M. Dapiaggi: *J. Solid State Chem.*, 2004, vol. 177, pp. 1713–16.
39. T. Langreiter and V. Kahlenberg: *Curr. Comput. Aid. Drug Des.*, 2015, vol. 5, pp. 143–53.
40. G.R. Holcomb: *Mater. High Temp.*, 2019, vol. 36, pp. 232–39.
41. Paolo Venturelli: *Am. Miner.*, 1999, pp. 895–904.
42. T. Saito: *Bull. Chem. Soc. Jpn.*, 1965, vol. 38, pp. 2008–009.
43. A.C. Turnock and H.P. Eugster: *J. Petrol.*, 1962, vol. 3, pp. 533–65.
44. L.A. Pérez-Maqueda, J.M. Criado, C. Real, J. Šubrt, and J. Boháček: *J. Mater. Chem.*, 1999, vol. 9, pp. 1839–46.
45. A. V. Roshchin and Vasily Roshchin: *Russ. Metall.*, 2003, pp. 1–5.
46. A. V. Roshchin and Vasily Roshchin: *Russ. Metall.*, 2003, pp. 97–102.